OPEN ACCESS

ARTICLE

Elevated melting temperature and superionic transition of H_2O ice

Meryem Berrada,[1,*] Keng-Hsien Chao,[1] Siheng Wang,[1] Dongzhou Zhang,[2] Vitali Prakapenka,[2] Stella Chariton,[2] Young Jay Ryu,[2] and Bin Chen[1,*]

*Correspondence: berrada@hawaii.edu (M.B.); binchen@hawaii.edu (B.C.)

Received: November 16, 2024; Accepted: August 15, 2025; Published Online: August 20, 2025; https://doi.org/10.59717/j.xinn-geo.2025.100154

© 2025 The Author(s). This is an open access article under the CC BY license (https://creativecommons.org/licenses/by/4.0/).

GRAPHICAL ABSTRACT

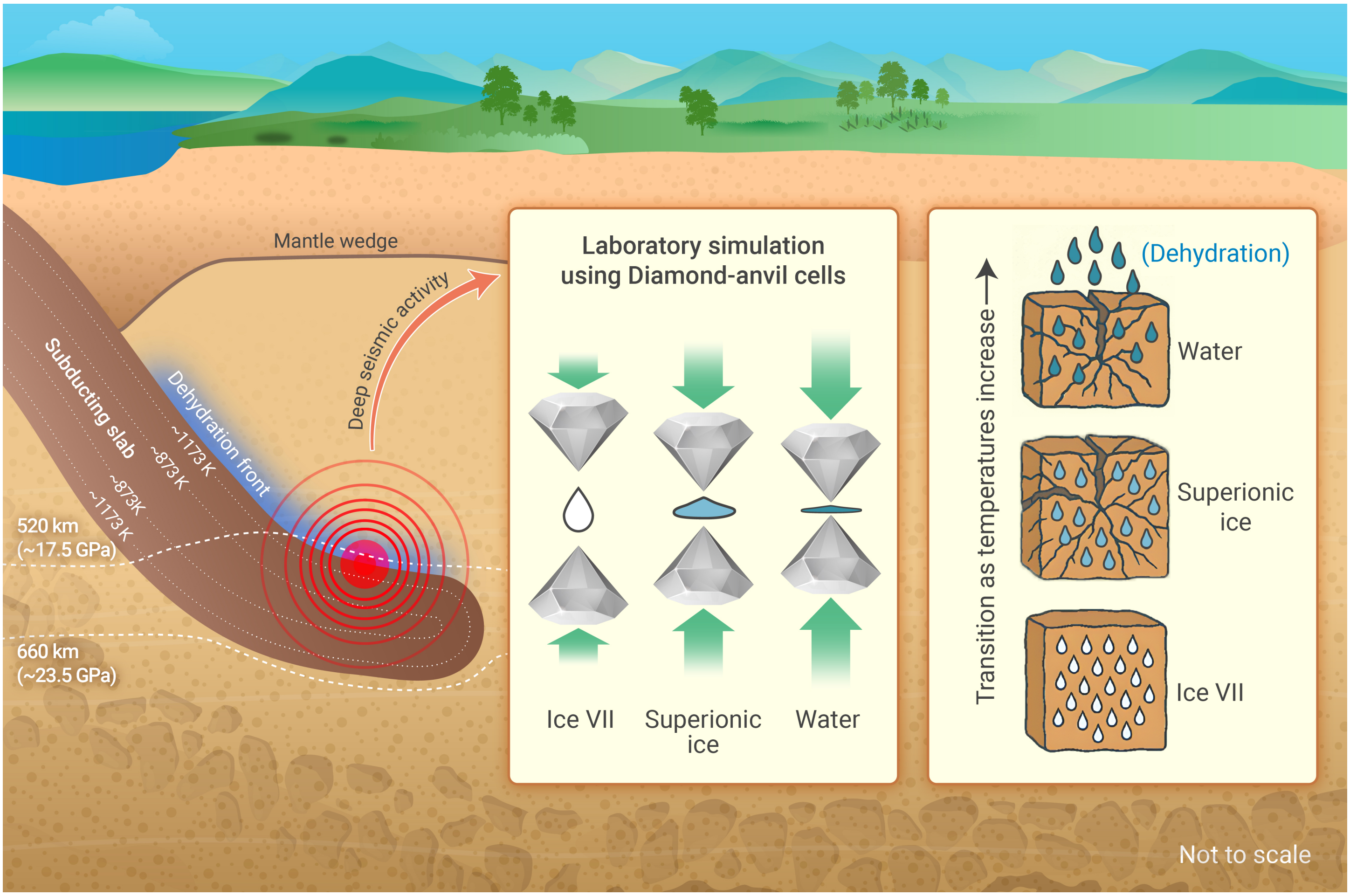

PUBLIC SUMMARY

- Superionic body-centered-cubic ice forms at ~9.5 GPa, a lower pressure than previously expected.
- Diamond anvil cell experiments mapped the elevated melting boundary of H_2O ice.
- Superionic ice in cold subducting slabs may affect deep Earth processes and contribute to deep earthquakes.

OPEN ACCESS

Elevated melting temperature and superionic transition of H_2O ice

Meryem Berrada,[1,*] Keng-Hsien Chao,[1] Siheng Wang,[1] Dongzhou Zhang,[2] Vitali Prakapenka,[2] Stella Chariton,[2] Young Jay Ryu,[2] and Bin Chen[1,*]

[1]Hawai'i Institute of Geophysics and Planetology, University of Hawai'i at Manoa, Honolulu 96822, USA

[2]Center for Advanced Radiation Sources, The University of Chicago, Chicago 60637, USA

*Correspondence: berrada@hawaii.edu (M.B.); binchen@hawaii.edu (B.C.)

Received: November 16, 2024; Accepted: August 15, 2025; Published Online: August 20, 2025; https://doi.org/10.59717/j.xinn-geo.2025.100154

© 2025 The Author(s). This is an open access article under the CC BY license (https://creativecommons.org/licenses/by/4.0/).

Citation: Berrada M., Chao K.-H., Wang S., et al. (2025). Elevated melting temperature and superionic transition of H_2O ice. *The Innovation Geoscience* **3**:100154.

Subduction of oceanic lithosphere effectively transports substantial amounts of water deep into the Earth, altering the properties of the surrounding mantle minerals and facilitating chemical interactions between the subducting lithosphere and mantle. Ice-VII is considered the stable phase of H_2O released from minerals within the cold subducting slabs by progressive dehydration. This study investigates the melting boundary of high-pressure ices and the transformation of ice-VII to superionic (SI) states under the specific pressure-temperature (*P*-*T*) conditions of subducting slabs. We conducted X-ray diffraction measurements on H_2O phases up to 42 GPa and 1400 K using a newly developed externally-heated diamond anvil cell system with precise *P*-*T* control. The experiments confirm the elevated melting temperature of high-pressure ice starting at 9.5 GPa, likely due to the appearance of SI body-centered cubic ice phase. The phase diagram of H_2O, particularly the elevated melting temperatures and transition to SI state, provides crucial insights into the role of water in cold subducting slabs and its possible association with deep-seated seismic activity and mantle dynamics.

INTRODUCTION

The phase diagram of ice encounters several structures: Ice Ih is the most common form of ice found on Earth's surface.[1] It has a hexagonal crystal structure and is stable at low pressures and temperatures. Ice II has a rhombohedral crystal structure and forms at higher pressures than ice Ih. With increasing pressures forms the tetragonal ice III, monoclinic ice V, tetragonal ice VI, and cubic ice VII. Ice VII is of particular interest because it is considered stable at conditions found in the cold subducting slabs and other extreme planetary environments.[2] Its equation of state (EoS) and melting boundary have been investigated at various pressures and temperatures.[2–9] Before melting at high pressures and temperatures, water transitions into the recently discovered superionic (SI) ice phase, which exhibits a unique combination of solid and liquid-like properties.[10,11] In this phase, the hydrogen atoms (protons) behave as if they were in a liquid state: They are highly mobile within a lattice of oxygen atoms that remains in a solid crystalline structure.[12,13] The high mobility of protons within the oxygen lattice results in a high ionic conductivity, comparable to that of liquid electrolytes.[14–16]

Understanding SI ices under high pressure-temperature conditions is essential for unraveling Earth's internal processes, especially the dynamics of subduction zones and the associated seismic activities. Although previous studies have extensively investigated the phase boundaries of high-pressure water ices, such as ice VII, the specific conditions under which SI ice forms within subducting slabs are still not well-defined.[5,12,17-24] In subduction zones, hydrous silicates carried into the mantle may release water under high pressures and temperatures.[25–27] The residual hydrous phases become denser than the surrounding mantle rock, allowing the hydrated material to continue sinking with the subducting slab.[28] When this hydrated material reaches the transition zone, located between 410 and 660 km beneath the Earth's surface, it encounters phase transitions in the mantle rock. These changes cause the hydrated material to stagnate due to changes in viscosity and rheology. Seismic studies have observed this stagnation as a decrease in the rate of subduction at these depths.[29–32] Deep-focus earthquakes occurring in this region are thought to result from mechanisms such as dehydration embrittlement, transformational faulting, and thermal runaway.[33] Dehydration embrittlement refers to the brittle fracture of the cold subduction slab caused by increased pore pressure following dehydration.[33] The released water interacts with surrounding mantle rocks, leading to complex chemical reactions, phase transitions, and mineralogical changes.[34–39] However, the stability and roles of water ices in these environments remain poorly constrained. This study aims to address these uncertainties by examining the structural transitions and melting behavior of high-pressure ices, with a specific focus on SI ice and its stability field.

Diamond anvil cells (DAC) combined with in-situ X-ray diffraction (XRD) measurements are commonly used to explore the properties and phase behavior of planetary materials. Traditionally, achieving high temperatures in DAC involved laser- or resistive-heating methods. While laser heating is widely used, it can introduce challenges such as temperature gradients, fluctuations, and control issues, resulting in chemical disparities.[40,41] On the other hand, external resistive heating offers uniform heating across the sample chamber which ensures stable temperature control and minimal fluctuations.[42] Leveraging the advantages of the externally-heated diamond anvil cell experimentation system (EH-DANCE), this study delves into the phase diagram of ice VII, aiming to resolve discrepancies in the melting boundary and the conditions of the SI-body-centered cubic (bcc) ice structure.[43]

MATERIALS AND METHODS

A total of 17 experiments were performed using BX90 DAC with 150-300 μm culet standard cut diamond anvils to investigate the phase diagram of ice VII up to 42 GPa and 1400 K. The EH-DANCE used a micro-heater made of sintered pyrophyllite donut-shaped ring and tungsten wires to provide resistive heating, while a type-K thermocouple was mounted near the culet to measure temperature (*T*). The sample chamber (75-120 μm in diameter depending on culet size) was laser cut in Re gaskets pre-indented to 40 μm thickness. It was then filled with a drop of deionized water and a piece of 5 μm thick gold foil. The equation of state (EoS) of gold was used as a pressure scale throughout the experiments.[44]

Characterization of the synthesized ice VII was performed at the 13-BMD beamline of the Advanced Photon Source at Argonne National Laboratory. The focused monochromatic X-ray beam (λ = 0.3344 Å) was 4x8 μm^2. The diffraction patterns of the step scans were collected with a Pilatus 1M detector. Rotation of the DAC (± 20°) was necessary to ensure that single-crystal diffraction peaks, if present, were not inadvertently missed during the assessment of melting. Measurements were taken at a 50 K interval, when possible, as *T* was controlled by the voltage applied to the heater. A vacuum environment, followed by a controlled nitrogen environment in the EH-DANCE, allowed achievements of simultaneously higher *T* and pressure (*P*) than those previously achieved with the apparatus. Data were analyzed using DIOPTAS software, while the lattice parameters were refined using PDIndexer software.[45,46] The 300 K data were fitted using the EoSFit7-GUI program.[47] The Pytheos package was then used to obtain the equations of state.[48] At 300 K, high temperature 3rd order Birch-Murnaghan EoS (HTBM3) is expressed as:

$$P(V,300K)=\frac{3}{2}K_0\left[\left(\frac{V_0}{V}\right)^{\frac{7}{3}}-\left(\frac{V_0}{V}\right)^{\frac{5}{3}}\right]\left[1+\frac{3}{4}(K_0-4)\left(\left(\frac{V_0}{V}\right)^{\frac{2}{3}}-1\right)\right] \quad (1)$$

where K_0 is the isothermal bulk modulus at 1 bar, K_0 is the pressure derivative of the bulk modulus, V is unit-cell volume, and V_0 is the zero-pressure unit-cell volume.[49] The temperature dependencies of the volume and bulk modulus are described as:

$$V(T)=V_0\left[1+\alpha_0(T-300)+\frac{1}{2}\alpha_1(T-300K)^2\right] \quad (2)$$

$$K(T)=K_0+\frac{dK}{dT}(T-300K) \quad (3)$$

where α_0 and α_1 are constants. In comparison, the Mie-Gruneisen-Debye EoS (MGD) incorporates the Debye model of specific heat, the Gruneisen parameter, and the Mie-Gruneisen parameter to describe the behavior of materials

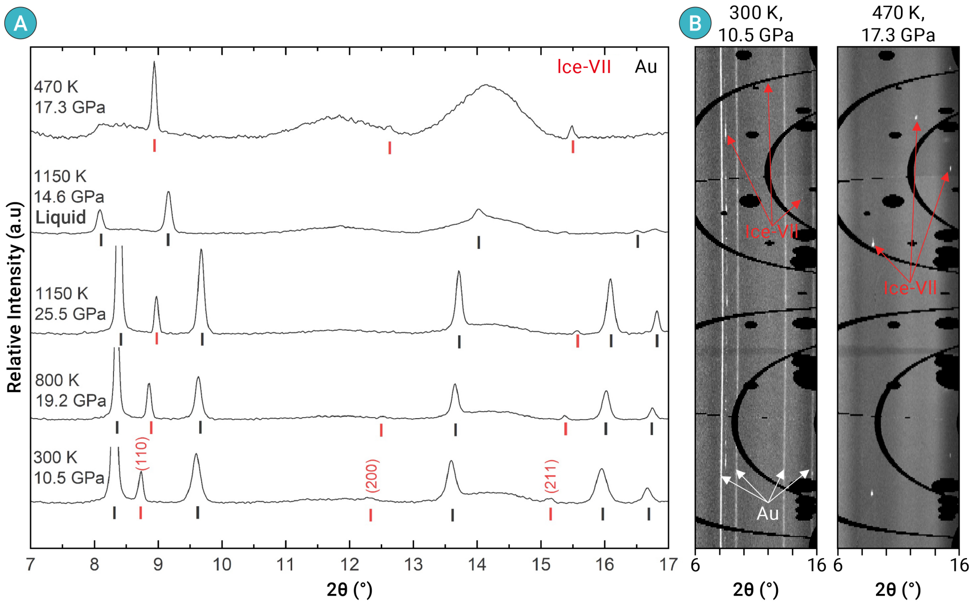

Figure 1. Representative X-ray diffraction data of ice-VII at high *P-T* conditions (A) Selected XRD patterns of ice VII with (B) "cake" representation of 2D XRD images at 300 K-10.5 GPa and 470 K-17.3 GPa.

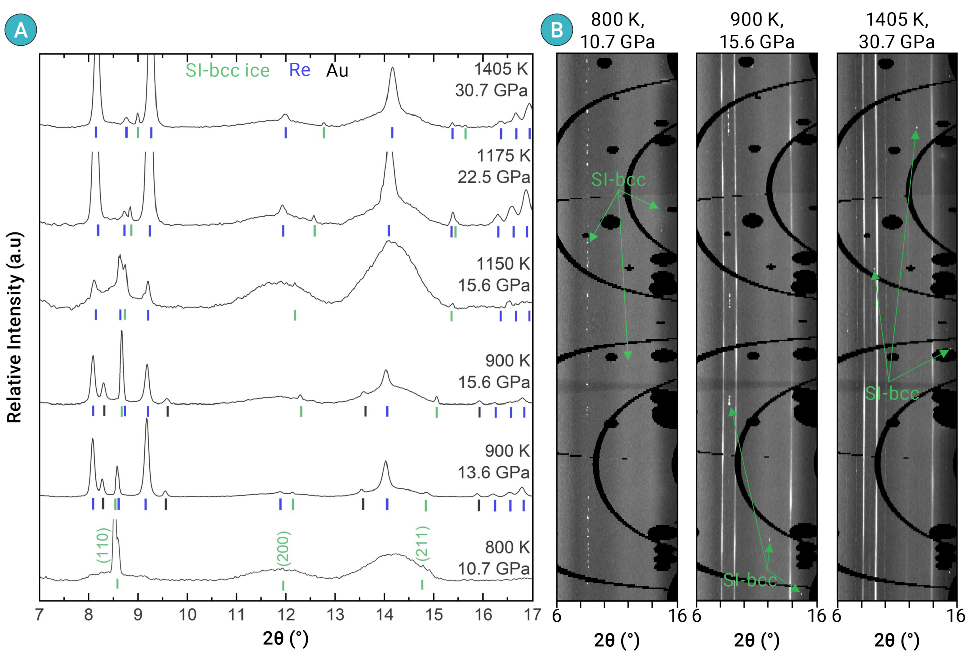

Figure 2. Representative X-ray diffraction data of SI-bcc ice at high *P-T* conditions (A) Selected XRD patterns of SI-bcc ice with (B) "cake" representation of 2D XRD images at 800 K-10.7 GPa, 900 K-15.6 GPa, and 1405 K-30.7 GPa.

under high-*P* and high-*T* conditions.[50,51] The Debye model describes the temperature dependence of the specific heat of a material based on the vibrational modes of its atoms.[52] The Gruneisen parameter and Mie-Gruneisen parameter account for thermal expansion and anharmonicity.[53,54] This model assumes separate terms for the ambient and high temperature pressures:

$$P(V,T) = P(V,300K) + \Delta P_{th}(V,T) \tag{4}$$

where $\Delta P_{th}(V,T)$ is expressed as:

$$\Delta P_{th}(V,T) = \frac{\gamma(V)}{V}\left[E_{th}(V,T) - E_{300K}(V,300K)\right] \tag{5}$$

where E_{th} describes the Debye model of vibrational energy, and γ_0 is the Grüneisen parameter, such that:

$$E_{th}(V,T) = 9nRT\left(\frac{T}{\theta_D}\right)^3 \int_0^{\frac{\theta_D}{T}} \left(\frac{x^3}{\exp(x)-1}\right) dx \tag{6}$$

using *n* as the number of atoms per unit formula, *R* as the gas constant, the Debye temperature $\Theta_{D,0}$ with $\theta_D = \theta_{D,0}\, exp\left[\frac{\gamma_0-\gamma}{q}\right]$ and $\gamma(V) = \gamma_0\left(\frac{V}{V_0}\right)^q$. Only $\Theta_{D,0}$ was fixed during fitting of the MGD EoS.

RESULTS

The characterization of ice VII involved a comprehensive examination of its *hkl* peaks, specifically (110), (200), and (211). Selected XRD patterns of ice VII are presented in Figure 1. As *T* was increased to approach the anticipated melting boundary at various *P* points, *P* also increased due to the thermal pressure. Once 1150 K was reached, *P* was slowly decreased until the sample was molten, as determined by the disappearance of the ice VII XRD peaks. Then, *P* was incrementally raised to observe the recrystallization of ice phases and to constrain the melting boundary. A noticeable increase in the sample *V* was observed in the sample peaks at several conditions during Runs #2, 8, and 11. As illustrated in Figure S1, this volume increase at 21 GPa aligns with literature reports of the SI-bcc ice.[12] It is worth noting that the exceptional fluidity of SI-bcc ice presents challenges in maintaining sample stability within the sample chamber at elevated temperatures. Selected XRD patterns of SI-bcc ice are presented in Figure 2.

The HTBM3 EoS of ice VII is presented in Figure 3. Table S1 presents the derived parameters for both the HTBM3 and MGD EoS models. Limited observations of SI-bcc ice lead to the perception of two distinct behaviors: A relatively steep compression curve below 25 GPa and a shallower one above 25 GPa. This disparity arises because the data above 25 GPa were collected at significantly higher *P* and *T*, resulting in higher volumes due to thermal expansion, which gives the EoS a shallower appearance. In contrast, the data below 25 GPa are obtained at relatively similar temperatures, providing a more accurate representation of the EoS of SI-bcc ice. In Figure S2, the standard parameters obtained from the HTBM3 EoS are compared with literature values.[2,3,5,7,9,55] Illustrating V/V_0 as a function of *P* provides valuable insights into the compressibility and phase transitions of materials under varying conditions. For ice VII, no phase transition is detected at 300 K up to ~ 30 GPa. While results from this study agree with most studies up to high pressures, see Table S1, some studies report a smaller V/V_0 thus a greater compressibility.[9,55]

The resulting phase diagram from this study is plotted in Figure 4A. The melting boundary, determined by the disappearance and re-appearance of the XRD peaks of ice within the sample chamber (see Figures S3 & S4), is well described by the Simon-Glatzel equation as $T_m = T_{ref}\left(\frac{P_m - P_{ref}}{a}+1\right)^b$, with the following parameters:

$$T_m^{<705K} = 353\,[K]\left(\frac{P_m - 1.90\,[GPa]}{1.65\,[GPa]}+1\right)^{0.40} \tag{7}$$

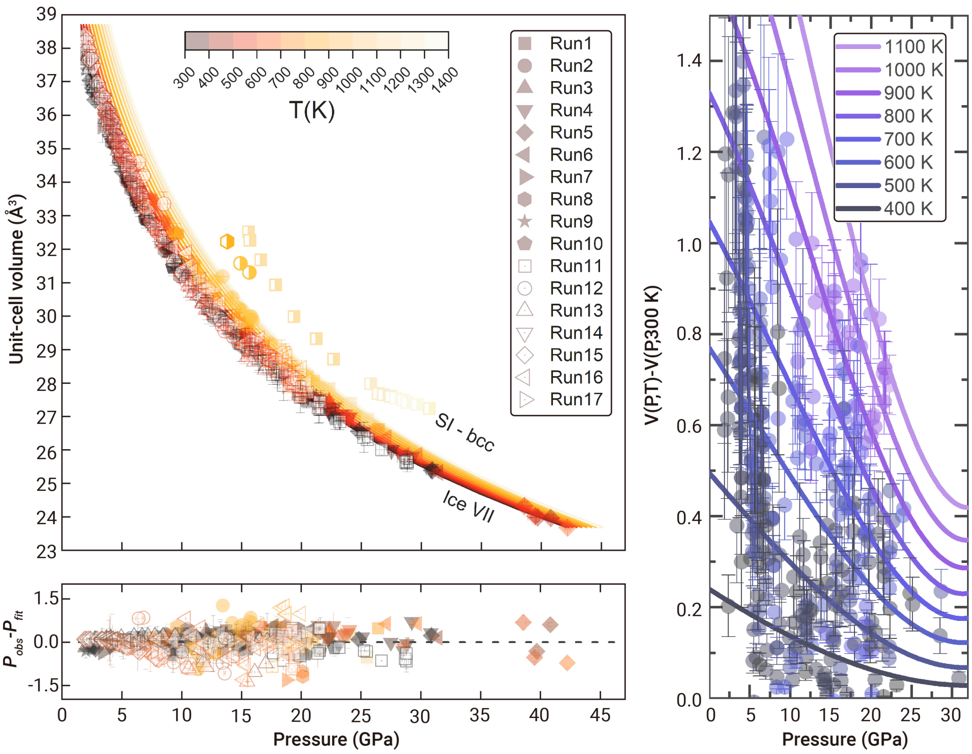

Figure 3. Equation of state following the HTBM3 models The half-filled symbols represent SI-bcc ice data from Runs #2, 8, and 11. The bottom figure shows the difference between the observed pressures from the gold standard and those obtained from the fits. The right figure shows the difference between the experimental volume at high T and that at 300 K, along with the corresponding fits. The resulting EoS parameters are V_0=41.5 ± 0.4 Å^3, K_0=17.0 ± 0.7 GPa, K_0'=5.3 ± 0.1, α_0=11×10^{-5} K^{-1}, α_1=16×10^{-8} K^{-2}, and dK/dT=-0.008 GPa/K.

$$T_m^{>705K} = 705\,[K]\left(\frac{P_m - 9.50\,[GPa]}{2.68\,[GPa]} + 1\right)^{0.39} \tag{8}$$

where P_m is the pressure at the melting point and T_m is the corresponding temperature. The reference pressure (P_{ref}) and temperature (T_{ref}) are fixed values based on experimental data, while parameters a and b are fitted to the data.

At 900 K, the transition from ice VII to the liquid phase aligns with previous measurements by Lai et al.[2] However, this study identifies SI-bcc ice immediately before melting at this temperature. Only two data points at 900 K show SI-bcc ice, while others indicate ice VII. These observations were made during Run #14 (see Figure S1), where temperature was increased to 900 K after reaching ~15 GPa at room temperature. SI-bcc ice peaks appeared at 15.6 GPa and again at 13.6 GPa during decompression. No SI-bcc was observed in subsequent measurements within the liquid state or during compression, suggesting that this phase emerges under specific conditions and is difficult to stabilize due to its reactive nature.

The SI-bcc ice phase boundary is determined by linearly interpolating the kink in melting boundary at 9.5 GPa-705 K with the high P-T SI-bcc ice observations. A change in the melting slope is typically indicative of a phase transition, similar to the ice VII to VII' transition above 40 GPa reported in the literature.[12,21,23] As shown in Figure 4, the change in melting slope near 9.5 GPa - 705 K coincides with previous reports of the SI phase near 15 GPa - 660 K,[21] 17 GPa - 880 K,[12] or 16 GPa - 810 K.[23] This kink has also been attributed to a molecular-to-ionic transition on the liquid side of the melting boundary, possibly caused by the ionization of H_2O to H^+ and OH^-.[19,56] Measurements of ice become noticeably more challenging beyond this transition due to increased sample leaking events at extremely high temperatures.

The high melting boundary identified here concurs with laser-heated DAC measurements from 20–90 GPa, as opposed to the lower boundaries reported in the literature.[5,17–20] Prakapenka et al.[12] and Schwager & Boehler[21] reported a similar elevated melting boundary, although the former recognized large temperature uncertainties, and the latter relied on visual observations.[12,21] As inferred by Prakapenka et al.,[12] the appearance of SI-bcc ice causes the melting boundary to rise more steeply, which is attributed to the higher entropy of SI-bcc ice compared to ice VII.

The discrepancies in the melting boundary likely stem from methodological differences, including heating techniques, pressure calibration, and temperature measurement uncertainties. The EH-DANCE system's bi-directional pressure control capability enabled precise bracketing of melting points at specific, discrete temperatures ranging from 400 K to 1100 K, which was achieved through one or multiple cycles of decompression and compression. The consistency of results across multiple runs and their agreement with previous studies at overlapping conditions indicate the accuracy of temperature measurements in this study and suggest overheating is unlikely to be an issue. The EH-DANCE experimental setup has been demonstrated to be particularly effective in constraining phase transitions under high P-T conditions,[43] leading to the determination of the stability field of SI-bcc ice phase and the observed elevated melting boundary of high-pressure ice. Furthermore, the positive slope of the ice VII to SI-bcc transition drawn in this study, although relying on a few data points, is aligned with the calculated melting trend from Hernandez & Caracas.[23]

Variability in reported SI-bcc ice conditions in the literature highlights a gap in the current understanding of ice's behavior under the extreme conditions of cold subducting slabs.[57] This range typically covers a significant portion of the Earth's mantle, which extends from the uppermost part to the deeper regions of the mantle. The outlined melting boundary of SI-bcc ice from this study reaches the P-T conditions of the cold subducting slab, in contrast to the previously reported lower melting boundaries.[5,17,19,22,58]

CONCLUSION

The phase diagram of ice, particularly the high melting temperatures of high-P ices, unveils intriguing insights into the behavior of water within the Earth's mantle. Understanding these transitions is essential for explaining deep-focus earthquakes, which have long been hypothesized to arise from structural instabilities within cold subducting slabs.[59] This study finds that the high melting boundary of ice and steep ice VII to SI-bcc ice transition raises the intriguing possibility of phase changes from ice-VII to SI-bcc ice or from SI-bcc ice to liquid within cold subducting slabs depending on the slab geotherms (Figure 4). In contrast, lower melting boundaries and shallow ice VII to SI-bcc ice transitions allow only liquid H_2O and, in some cases, SI ice in subducting slabs.

The complex scenario presented here has profound implications for mantle dynamics. Solid ice VII and SI ice in cold slabs could trap H_2O molecules within their crystal structures, enabling water to descend deeper into the mantle.[25] Hot subducting slabs would only contain liquid water under the same conditions, while very cold slabs would only contain ice VII, resulting in no phase transitions that could potentially be related to deep-focus seismic events. On the other hand, deep-focus seismic events may be triggered by the release of water from hydrous minerals at great depths. For example, several hydrous minerals such as phase Egg ($AlSiO_3OH$),[60] dense hydrous magnesium silicates (DHMS) including Phase D ($MgSi_2H_2O_6$)[61,62] and Phase H ($MgSiO_4H_2$),[63,64] Topaz-OH ($Al_2SiO_4(OH)_2$),[65] and OH-bearing nominally anhydrous minerals such as wadsleyite (Mg_2SiO_4)[66–68] and ringwoodite (Mg_2SiO_4)[67–69] can act as significant water reservoirs within the mantle transition zone. These phases are stable under extreme P-T conditions, with some, like phase Egg and DHMS, remaining stable beyond the SI-bcc transition and the ice melting boundary defined in this study. This delayed melting of ice and potential release of water from hydrous minerals suggests that water may indeed be carried to greater depths in the cold subducting slabs, potentially leading to fluid-triggered deep-focus earthquakes between 520-660 km at ~20 - 26 GPa,[33,70] as well as the precipitation of sublithospheric diamonds.[71] This underlines the necessity for more comprehensive experimental data to better understand the phase behavior of ice under extreme conditions that resemble those within planets.

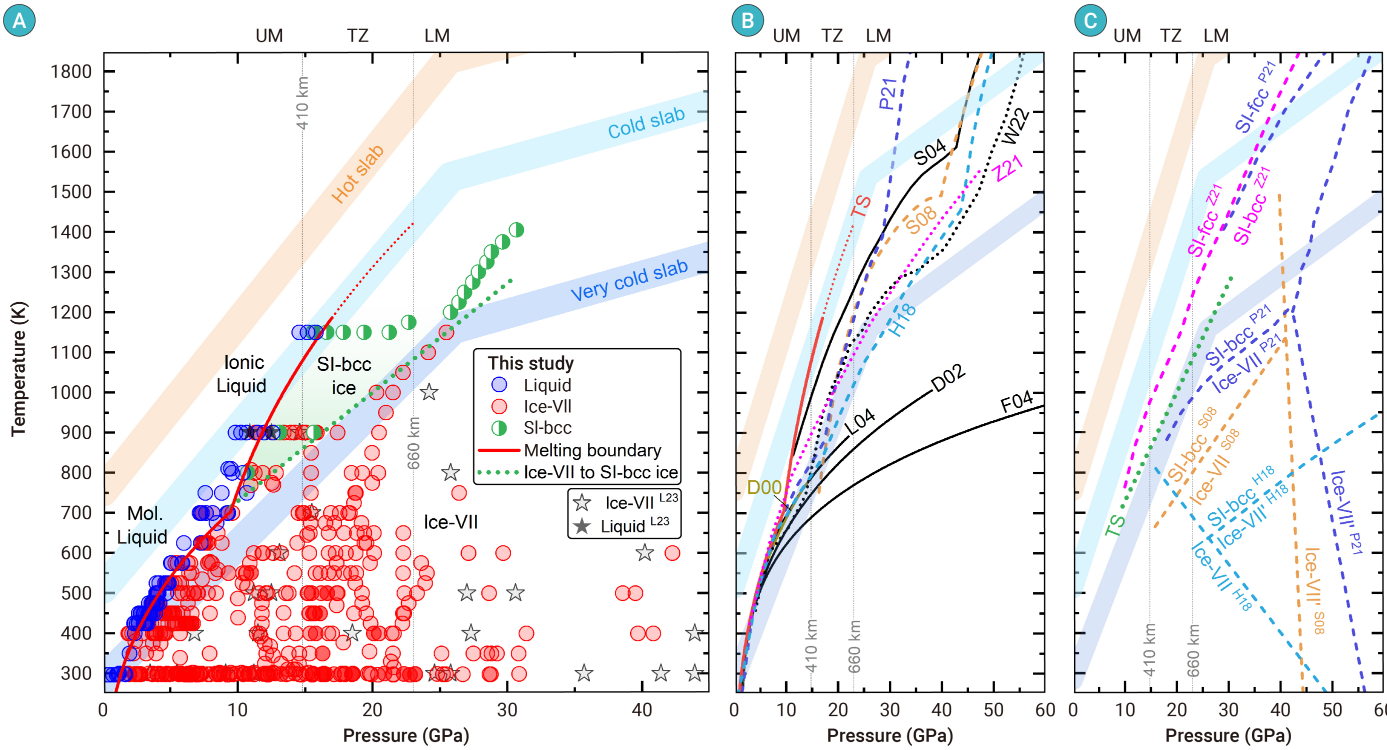

Figure 4. Phase diagram of H_2O ice, superimposed on the *P-T* conditions of subducting slabs and compared with literature results (A) The ice VII and SI-bcc ice results from this study compared to another experimental study which used the same method and procedure (L23, Lai et al.[2]). The solid red line represents the melting boundary identified in this study. The dotted green line illustrates the estimated Ice-VII to SI-bcc ice transition. The molecular-to-ionic liquid transition is also displayed.[19,56] (B) Reported melting boundaries. (C) Reported solid-solid transitions. The very cold, cold, and hot subducting slab *P-T* conditions are illustrated by the shaded area.[57] TS refers to this study, D00 refers to Datchi et al.,[17] D02 refers to Dubrovinskaia and Dubrovinsky,[18] F04 refers to Frank et al.,[5] L04 refers to Lin et al.,[19] P21 refers to Prakapenka et al.,[12] S04 refers to Schwager et al.,[20] S08 refers to Schwager and Boehler,[21] W22 refers to Weck et al.,[22] H18 refers to Hernandez and Caracas,[23] and Z21 refers to Zhang et al.[24] The 410 and 660 km lines refer to the seismic discontinuities in the mantle separating the upper mantle (UM), transition zone (TZ), and lower mantle (LM).

REFERENCES

1. Salzmann C. G. (2019). Advances in the experimental exploration of water's phase diagram. *J. Chem. Phys.* **150**:060901. DOI:10.1063/1.5085163
2. Lai X., Zhu F., Zhang D., et al. (2023). Thermal equation of state of ice-VII revisited by single-crystal X-ray diffraction. *Am. Mineral.* **108**:1530–1537. DOI:10.2138/am-2022-8554
3. Fei Y., Mao H. and Hemley R. J. (1993). Thermal expansivity, bulk modulus, and melting curve of H_2O–ice VII to 20 GPa. *J. Chem. Phys.* **99**:5369–5373. DOI:10.1063/1.465980
4. Sugimura E., Komabayashi T., Hirose K., et al. (2010). Simultaneous high-pressure and high-temperature volume measurements of ice VII and its thermal equation of state. *Phys. Rev. B.* **82**:134103. DOI:10.1103/PhysRevB.82.134103
5. Frank M. R., Fei Y. and Hu J. (2004). Constraining the equation of state of fluid H_2O to 80 GPa using the melting curve, bulk modulus, and thermal expansivity of Ice VII. *Geochim. Cosmochim. Acta.* **68**:2781–2790. DOI:10.1016/j.gca.2003.12.007
6. Somayazulu M., Shu J., Zha C., et al. (2008). In situ high-pressure x-ray diffraction study of H_2O ice VII. *J. Chem. Phys.* **128**:064510. DOI:10.1063/1.2813890
7. Hemley R. J., Jephcoat A. P., Mao H. K., et al. (1987). Static compression of H_2O-ice to 128 GPa (1.28 Mbar). *Nature* **330**:737–740. DOI:10.1038/330737a0
8. Liu L. (1982). Compression of ice VII to 500 kbar. *Earth Planet. Sci. Lett.* **61**:359–364. DOI:10.1016/0012-821X(82)90066-8
9. Wolanin E., Pruzan Ph., Chervin J. C., et al. (1997). Equation of state of ice VII up to 106 GPa. *Phys. Rev. B* **56**:5781–5785. DOI:10.1103/PhysRevB.56.5781
10. Redmer R., Mattsson T. R., Nettelmann N., et al. (2011). The phase diagram of water and the magnetic fields of Uranus and Neptune. *Icarus* **211**:798–803. DOI:10.1016/j.icarus.2010.08.008
11. Sun J., Clark B. K., Torquato S., et al. (2015). The phase diagram of high-pressure superionic ice. *Nat. Commun.* **6**:8156. DOI:10.1038/ncomms9156
12. Prakapenka V. B., Holtgrewe N., Lobanov S. S., et al. (2021). Structure and properties of two superionic ice phases. *Nat. Phys.* **17**:1233–1238. DOI:10.1038/s41567-021-01351-8
13. Hernandez J.A. and Caracas R. (2016). Superionic–superionic phase transitions in body-centered cubic H_2O ice. *Phys. Rev. Lett.* **117**:135503. DOI:10.1103/PhysRevLett.117.135503
14. Sugimura E., Komabayashi T., Ohta K., et al. (2012). Experimental evidence of superionic conduction in H_2O ice. *J. Chem. Phys.* **137**:194505. DOI:10.1063/1.4766816
15. Guo Z., Wang T., Wei H., et al. (2019). Ice as solid electrolyte to conduct various kinds of ions. *Angew. Chem. Int. Ed.* **58**:12569–12573. DOI:10.1002/anie.201907832
16. Millot M., Hamel S., Rygg J. R., et al. (2018). Experimental evidence for superionic water ice using shock compression. *Nat. Phys.* **14**:297–302. DOI:10.1038/s41567-017-0017-4
17. Datchi F., Loubeyre P. and LeToullec R. (2000). Extended and accurate determination of the melting curves of argon, helium, ice H_2O and hydrogen H_2. *Phys. Rev. B.* **61**:6535–6546. DOI:10.1103/PhysRevB.61.6535
18. Dubrovinskaia N. and Dubrovinsky L. (2002). Melting curve of water studied in externally heated diamond-anvil cell. *High Press. Res.* **23**:307–311. DOI:10.1080/0895795031000139226
19. Lin J. F., Militzer B., Struzhkin V. V., et al. (2004). High pressure-temperature Raman measurements of H_2O melting to 22 GPa and 900 K. *J. Chem. Phys.* **121**:8423–8427. DOI:10.1063/1.1784438
20. Schwager B., Chudinovskikh L., Gavriliuk A., et al. (2004). Melting curve of H_2O to 90 GPa measured in a laser-heated diamond cell. *J. Phys.: Condens. Matter* **16**:S1177. DOI:10.1088/0953-8984/16/14/028
21. Schwager B. and Boehler R. (2008). H_2O: Another ice phase and its melting curve. *High Press. Res.* **28**:431–433. DOI:10.1080/08957950802347973
22. Weck G., Queyroux J.A., Ninet S., et al. (2022). Evidence and stability field of fcc superionic water ice using static compression. *Phys. Rev. Lett.* **128**:165701. DOI:10.1103/PhysRevLett.128.165701
23. Hernandez J.A. and Caracas R. (2018). Proton dynamics and the phase diagram of dense water ice. *J. Chem. Phys.* **148**:214501. DOI:10.1063/1.5028389
24. Zhang L., Wang H., Car R., et al. (2021). Phase diagram of a deep potential water model. *Phys. Rev. Lett.* **126**:236001. DOI:10.1103/PhysRevLett.126.236001
25. Karato S., Karki B. and Park J.. (2020). Deep mantle melting, global water circulation and its implications for the stability of the ocean mass. *Prog. Earth Planet. Sci.* **7**:76. DOI:10.1186/s40645-020-00379-3
26. Liu Z., Park J. and Karato S. (2018). Seismic evidence for water transport out of the mantle transition zone beneath the European Alps. *Earth Planet. Sci. Lett.* **482**:93–104. DOI:10.1016/j.epsl.2017.10.054
27. Ni H., Zhang L. and Guo X. (2016). Water and partial melting of Earth's mantle. *Sci. China Earth Sci.* **59**:720–730. DOI:10.1007/s11430-015-5254-8
28. Liu Z., Park J. and Karato S. (2016). Seismological detection of low-velocity anomalies surrounding the mantle transition zone in Japan subduction zone. *Geophys. Res. Lett.* **43**:2480–2487. DOI:10.1002/2015GL067097
29. Ohtani E. and Zhao D. (2009). The role of water in the deep upper mantle and transition zone: Dehydration of stagnant slabs and its effects on the big mantle wedge. *Russ. Geol. Geophys.* **50**:1073–1078. DOI:10.1016/j.rgg.2009.11.006

www.the-innovation.org/geoscience

30. Tauzin B., Kim S. and Kennett B. L. N. (2017). Pervasive seismic low-velocity zones within stagnant plates in the mantle transition zone: Thermal or compositional origin. *Earth Planet. Sci. Lett.* **477**:1–13. DOI:10.1016/j.epsl.2017.08.006
31. Lai Y., Chen L., Wang T., et al. (2019). Mantle transition zone structure beneath Northeast Asia from 2-D triplicated waveform modeling: Implication for a segmented stagnant slab. *J. Geophys. Res. Solid Earth* **124**:1871–1888. DOI:10.1029/2018JB016642
32. Goes S., Agrusta R., van Hunen J., et al. (2017). Subduction-transition zone interaction: A review. *Geosphere* **13**:644–664. DOI:10.1130/GES01476.1
33. Zhan Z. (2020). Mechanisms and implications of deep earthquakes. *Annu. Rev. Earth Planet. Sci.* **48**:147–174. DOI:10.1146/annurev-earth-053018-060314
34. Cai N. and Wang D. (2022). Sound velocity of $(Mg_{0.91}Fe_{0.09})_2SiO_4$ wadsleyite and its implications to water distribution in mantle transition zone. *Geophys. Res. Lett.* **49**:e2022GL100302. DOI:10.1029/2022GL100302
35. Das T., Chatterjee S., and Saha-Dasgupta T. (2022). First-principles study of water incorporation in Fe-containing wadsleyite. *Phys. Earth Planet. Inter.* **333**:106940. DOI:10.1016/j.pepi.2022.106940
36. Kim H., Lee Y., Kim D., et al. (2022). Roles of partial hydration of mantle transition zone and wadsleyite–olivine phase transition in wet plume development: Origin of quaternary intraplate volcanoes in Korea. *Tectonophysics* **837**:229467. DOI:10.1016/j.tecto.2022.229467
37. Miladinova I., Kurz W., and Hilmbauer-Hofmarcher T. (2023). Fluid–mantle interaction along the Mariana convergent margin. *Geochem. Geophys. Geosyst.* **24**:e2023GC010968. DOI:10.1029/2023GC010968
38. Wang Z. and Wang Y. (2022). Global water distribution in the mantle transition zone from a seismic isotropic velocity model and mineral physics modeling. *Front. Earth Sci. (Lausanne)* **10**. DOI:10.3389/feart.2022.984063
39. Zelenski M., Plyasunov A. V., Kamenetsky V. S., et al. (2022). High-temperature water–olivine interaction and hydrogen liberation in the subarc mantle. *Contrib. Mineral. Petrol.* **177**:47. DOI:10.1007/s00410-022-01910-z
40. Mezouar M., Giampaoli R., Garbarino G., et al. (2017). Methodology for in situ synchrotron X-ray studies in the laser-heated diamond anvil cell. *High Press. Res.* **37**:170–180. DOI:10.1080/08957959.2017.1306626
41. Andrault D. and Fiquet G. (2001). Synchrotron radiation and laser heating in a diamond anvil cell. *Rev. Sci. Instrum.* **72**:1283–1288. DOI:10.1063/1.1343866
42. Yan J., Doran A., MacDowell A. A., et al. (2021). A tungsten external heater for BX90 diamond anvil cells with a range up to 1700 K. *Rev. Sci. Instrum.* **92**:013903. DOI:10.1063/5.0009663
43. Wang S., Berrada M., Chao K.H., et al. (2023). Externally-heated diamond anvil cell experimentation (EH-DANCE) for studying materials and processes under extreme conditions. *Rev. Sci. Instrum.* **94**:123902. DOI:10.1063/5.0180103
44. Fei Y., Ricolleau A., Frank M., et al. (2007). Toward an internally consistent pressure scale. *Proc. Natl. Acad. Sci. U.S.A.* **104**:9182–9186. DOI:10.1073/pnas.0609013104
45. Seto Y., Nishio-Hamane D., Nagai T., et al. (2010). Development of a software suite on X-ray diffraction experiments. *Rev. High Press. Sci. Technol.* **20**:269–276. DOI:10.4131/jshpreview.20.269
46. Prescher C. and Prakapenka V. B. (2015). DIOPTAS: A program for reduction of two-dimensional X-ray diffraction data and data exploration. *High Press. Res.* **35**:223–230. DOI:10.1080/08957959.2015.1059835
47. Gonzalez-Platas J., Alvaro M., Nestola F., et al. (2016). EosFit7-GUI: A new graphical user interface for equation of state calculations, analyses and teaching. *J. Appl. Crystallogr.* **49**:1377–1382. DOI:10.1107/S1600576716008050
48. Shim D. (2017). Pytheos – A Python tool set for equations of state. Zenodo. DOI: 10.5281/zenodo.802392
49. Birch F. (1952). Elasticity and constitution of the Earth's interior. *J. Geophys. Res. (1896–1977)* **57**:227–286. DOI:10.1029/JZ057i002p00227
50. Jackson I. and Rigden S. M. (1996). Analysis of P–V–T data: Constraints on the thermoelastic properties of high-pressure minerals. *Phys. Earth Planet. Inter.* **96**:85–112. DOI:10.1016/0031-9201(96)03143-3
51. Pankov L. V., Ullmann W., Heinrich R., et al. (1998). Thermodynamics of deep geophysical media. *Russ. J. Earth Sci.* **1**:11–49. DOI:10.2205/1998ES000002
52. Debye P. (1912). Zur theorie der spezifischen wärmen. *Ann. Phys.* **344**:789–839. DOI:10.1002/andp.19123441404
53. Grüneisen E. (1912). Theorie des festen zustandes einatomiger elemente. *Ann. Phys.* **344**:257–306. DOI:10.1002/andp.19123441202
54. Grüneisen E. (1908). Über die thermische ausdehnung und die spezifische wärme der metalle. *Ann. Phys.* **331**:211–216. DOI:10.1002/andp.19083310611
55. Bezacier L., Journaux B., Perrillat J.P., et al. (2014). Equations of state of ice VI and ice VII at high pressure and high temperature. *J. Chem. Phys.* **141**:104505. DOI:10.1063/1.4894421
56. Holmes N. C., Nellis W. J., Graham W. B., et al. (1985). Spontaneous Raman scattering from shocked water. *Phys. Rev. Lett.* **55**:2433. DOI:10.1103/PhysRevLett.55.2433
57. Maeda F., Ohtani E., Kamada S., et al. (2017). Diamond formation in the deep lower mantle: A high-pressure reaction of $MgCO_3$ and SiO_2. *Sci. Rep.* **7**:40602. DOI:10.1038/srep40602
58. Dubrovinskaia N. and Dubrovinsky L. (2003). Whole-cell heater for the diamond anvil cell. *Rev. Sci. Instrum.* **74**:3433–3437. DOI:10.1063/1.1578151
59. Sobisevich L. E., Sobisevich A. L. and Kanonidi K. Kh. (2014). Mechanism of source formation of deep focus earthquakes. *Dokl. Earth Sci.* **459**:1391–1396. DOI:10.1134/S1028334X14110063
60. Fukuyama K., Ohtani E., Shibazaki Y., et al. (2017). Stability field of phase Egg, $AlSiO_3OH$ at high pressure and high temperature: Possible water reservoir in mantle transition zone. *J. Mineral. Petrol. Sci.* **112**:31–35. DOI:10.2465/jmps.160719e
61. Shieh S. R., Mao H., Hemley R. J., et al. (1998). Decomposition of phase D in the lower mantle and the fate of dense hydrous silicates in subducting slabs. *Earth Planet. Sci. Lett.* **159**:13–23. DOI:10.1016/S0012-821X(98)00062-4
62. Frost D. J. and Fei Y. (1998). Stability of phase D at high pressure and high temperature. *J. Geophys. Res. Solid Earth* **103**:7463–7474. DOI:10.1029/98JB00077
63. Nishi M., Irifune T., Tsuchiya J., et al. (2014). Stability of hydrous silicate at high pressures and water transport to the deep lower mantle. *Nat. Geosci.* **7**:224–227. DOI:10.1038/ngeo2074
64. Tsuchiya J. and Mookherjee M. (2015). Crystal structure, equation of state and elasticity of phase H ($MgSiO_4H_2$) at Earth's lower mantle pressures. *Sci. Rep.* **5**:15534. DOI:10.1038/srep15534
65. Mookherjee M., Tsuchiya J. and Hariharan A. (2016). Crystal structure, equation of state, and elasticity of hydrous aluminosilicate phase, topaz-OH ($Al_2SiO_4(OH)_2$) at high pressures. *Phys. Earth Planet. Inter.* **251**:24–35. DOI:10.1016/j.pepi.2015.11.006
66. Grützner T., Klemme S., Rohrbach A., et al. (2018). The effect of fluorine on the stability of wadsleyite: Implications for the nature and depths of the transition zone in the Earth's mantle. *Earth Planet. Sci. Lett.* **482**:236–244. DOI:10.1016/j.epsl.2017.11.011
67. Tsujino N., Yoshino T., Yamazaki D., et al. (2019). Phase transition of wadsleyite–ringwoodite in the Mg_2SiO_4–Fe_2SiO_4 system. *Am. Mineral.* **104**:588–594. DOI:10.2138/am-2019-6823
68. Wang W. and Wu Z. (2022). A first-principles study of water in wadsleyite and ringwoodite: Implication for the 520 km discontinuity. *Am. Mineral.* **107**:1361–1368. DOI:10.2138/am-2021-7929
69. Zhou W.Y., Zhang J. S., Huang Q., et al. (2022). High pressure–temperature single-crystal elasticity of ringwoodite: Implications for detecting the 520 discontinuity and metastable ringwoodite at depths greater than 660 km. *Earth Planet. Sci. Lett.* **579**:117359. DOI:10.1016/j.epsl.2021.117359
70. Qiu R., Zeng Q., Wang H., et al. (2023). Anomalous thermal transport across the superionic transition in ice. *Chin. Phys. Lett.* **40**:116301. DOI:10.1088/0256-307X/40/11/116301
71. Shirey S. B., Wagner L. S., Walter M. J., et al. (2021). Slab transport of fluids to deep focus earthquake depths—Thermal modeling constraints and evidence from diamonds. *AGU Adv.* **2**:e2020AV000304. DOI:10.1029/2020AV000304

FUNDING AND ACKNOWLEDGMENTS

The authors are grateful to Dr. Yoshiyuki Okuda for his insightful communications and invaluable contributions, which greatly enriched this work. This work was supported by funds to M.B. from the Natural Sciences and Engineering Research Council of Canada [PDF – 567732 – 2022] and the Fonds de Recherche Nature et Technologies du Quebec [B3X 317379] and by funds to B.C. from the National Science Foundation [EAR-1829273 and EAR-2127807], NASA [80NSSC22K0138], and Petroleum Research Fund from American Chemical Society (67782-ND8). Portions of this work were carried out at GeoSoilEnviroCARS (The University of Chicago, Sector 13), Advanced Photon Source, Argonne National Laboratory. GeoSoilEnviroCARS is supported by the National Science Foundation-Earth Sciences (EAR-1634415). This research used resources of the Advanced Photon Source, a U.S. Department of Energy (DOE) Office of Science User Facility operated for the DOE Office of Science by Argonne National Laboratory under Contract No. DE-AC02-06CH11357. The funders had no role in study design, data collection and analysis, decision to publish, or preparation of the manuscript.

AUTHOR CONTRIBUTIONS

B.C. conceived the idea and designed the research. M.B. and B.C. analyzed the data. All authors performed the experiments. All authors contributed to the manuscript and approved the final version.

DECLARATION OF INTERESTS

The authors declare no competing interests.

DATA AND CODE AVAILABILITY

All experimental data are available in Supporting Information – Appendix 2.

SUPPLEMENTAL INFORMATION

It can be found online at https://doi.org/10.59717/j.xinn-geo.2025.100154